China Geology 9 (2026) 243−256

China Geology

Journal homepage: http://chinageology.cgs.cn
https://www.sciencedirect.com/journal/china-geology

Destruction of the North China Craton: Evidence from the electrical structure and fluid content

Bao-chun Li[a, b], Gao-feng Ye[a,*], Shao-huai Sun[b], Le-tian Zhang[a], Sheng Jin[b], Wen-bo Wei[a], Hao Dong[a]

[a] *School of Geophysics and Information Technology, China University of Geosciences (Beijing), Beijing* 100083, *China*
[b] *School of Resources and Environmental Engineering, Inner Mongolia University of Technology, Hohhot* 010051, *China*

A R T I C L E I N F O

Article history:
Received 11 March 2024
Received in revised form 11 November 2024
Accepted 19 March 2025
Available online 2 April 2025

Keywords:
Craton rifting
Upper mantle electrical structure
Temperature
Mantle fluid
Water amd carbon dioxide
Melt fraction
Volatile
Xenolith
North China Craton
Geological survey engineering

A B S T R A C T

The three-dimensional resistivity model of the lithosphere and fluid content plays a significant role in analyzing the spatiotemporal distribution and dynamic reasons for the North China Craton (NCC) destruction. The conductivity is related to temperature and melt fraction using laboratory experiments. The Hashin-Shtrikman (*HS*) bounds are used to constrain the conductivity range of rocks in the solid and solid-melt systems. The authors established the lithospheric conductivity-temperature relationship by combining the mineral composition obtained from the analysis of xenoliths, the steady-state heat conduction equation, water, and carbon dioxide. To discuss the destruction of the NCC, the three-dimensional resistivity structure model obtained from the magnetotelluric sounding (MT) array inversion of the NCC is compared with the model calculated using the *HS* bounds. The research results show that the higher the volatile water and carbon dioxide content in the fluid, the lower the mantle solidus. Based on the melt fractions of the Ordos Block, Trans-North China Orogen, and Bohai Bay Basin, the speculated lithosphere-asthenosphere boundary (LAB) exhibits the characteristics of deep in the west and shallow in the east. The partial melting of the Bohai Bay Basin began at a shallower depth than other places, with a more significant difference in fluid content in the depth.

©2026 China Geology Editorial Office.

1. Introduction

The North China Craton (NCC) is bordered to the north by the Central Asian Orogenic Belt, to the south by the Qinling–Dabie Orogen and the South China Block, and to the east by the Bohai Sea and the Yellow Sea (Fig. 1). It is generally believed that the Eastern and Western blocks of the NCC collided and amalgamated along the Trans-North China Orogen in the Early Paleoproterozoic, forming the unified basement (Zhao GC et al., 2001; Zhai MG and Santosh M, 2011). From 220 Ma, the Paleo-Pacific plate subducted westward (Menzies MA, 1993; Deng JF et al., 1994; Xu YG et al., 2004; Niu YL, 2005; Wu FY et al., 2005, 2011; Zhang HF et al., 2007; Gao S et al., 2009; Su JB et al., 2014), and retreated after 140 Ma (Wilde SA, 2015), resulting in significant lithospheric thinning in the Eastern Block. From 55 Ma, the collision between the Indian Plate and the Eurasian Plate (Yin A and Harrison TM, 2000) has led to the southwest trending compressive forces associated with the uplift of the Qinghai-Xizang Plateau, which has affected the Western Block (Chen XB et al., 2011). Previous studies have mostly suggested that the lithosphere in the Eastern Block has been significantly thinned, the Trans-North China Orogen has been reconfigured, and the Western Block has remained stable (Zhu RX et al., 2012). Combining the results of previous studies, it can be inferred that the lithospheric thinning, large-scale magmatic activity, and structural deformation in the NCC merely manifest its evolutionary process. These are attributed to fundamental changes in the lithospheric mantle's material composition and physicochemical properties, disrupting the craton's inherent stability (Yang YH et al., 2009; Zhu RX and Xu YG, 2019). Therefore, investigating the lithospheric structure is of significant scientific importance for understanding the North China Craton's destruction.

The magnetotelluric sounding (MT) method method

First author: *E-mail address*: libaochun@imut.edu.cn (Bao-chun Li).

* Corresponding author: *E-mail address*: ygf@cugb.edu.cn (Gao-feng Ye).

Literary editor: Xi-jie Chen
doi:10.31035/cg2024038
2096-5192/© 2026 China Geology Editorial Office.

Copyright © 2026 Editorial Office of China Geology. Publishing services by Elsevier B.V. on behalf of KeAi Communications Co. Ltd.
This is an open access article under the CC BY-NC-ND License (http://creativecommons.org/licenses/by-nc-nd/4.0/).

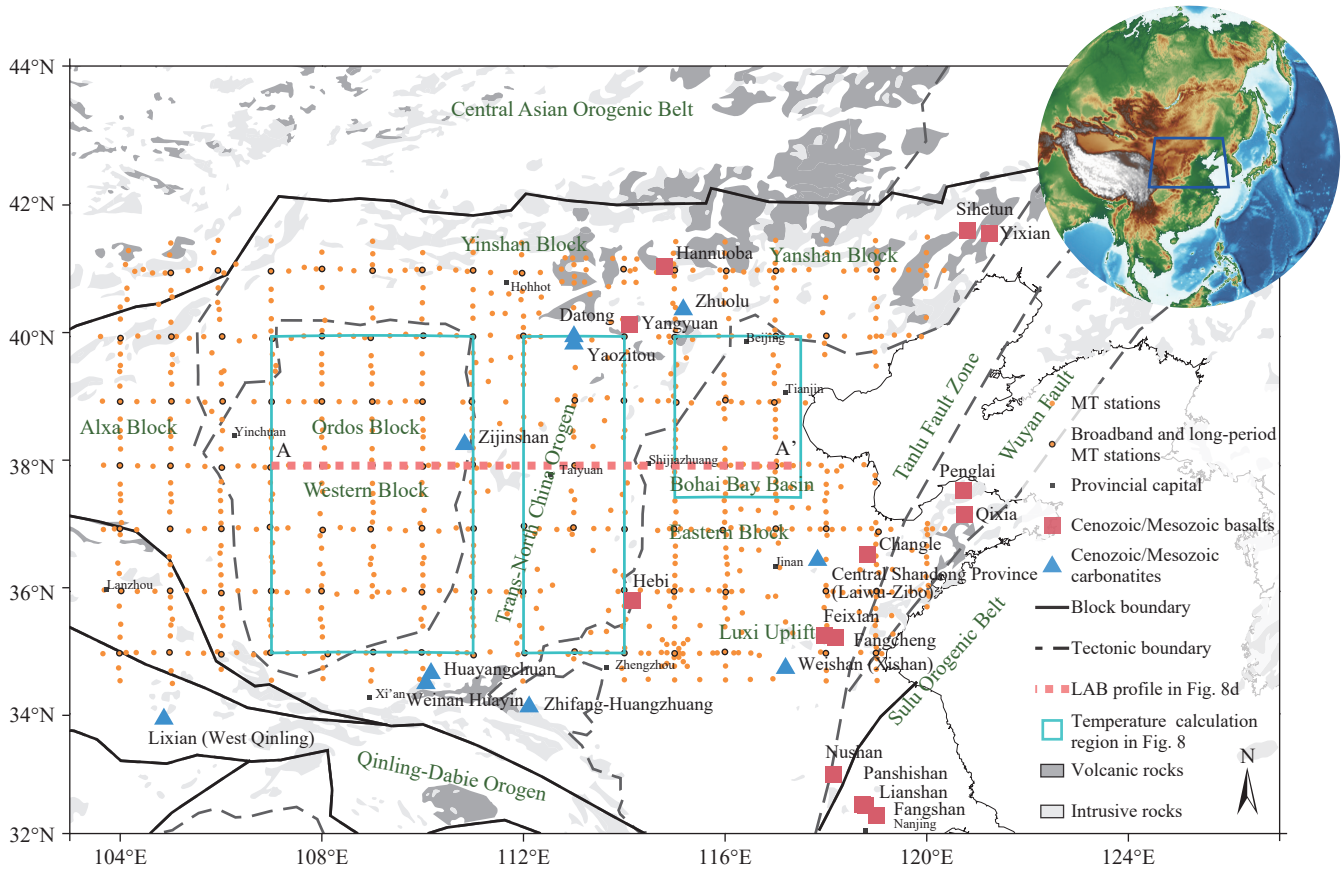

Fig. 1. Simplified tectonic map of the NCC and distribution of MT array stations (after Li BC et al., 2019; Ye GF et al., 2024).

measures natural electromagnetic signals at different frequencies to obtain the electrical structure of the crust and upper mantle. Previous research in the NCC has involved the crustal and upper mantle resistivity models through MT profiles and arrays, with interpretations of the resistivity anomalies (Wei WB et al., 2002; Dong H et al., 2014; Ye GF et al., 2021; Huang JH et al., 2022). In the Eastern Block, the high-resistivity anomalies in the Yanshan Block on the northern Bohai Bay Basin represent residual ancient cratonic lithosphere. In contrast, the extensive low-resistivity anomalies in the lower crust and upper mantle indicate the upwelling of asthenospheric material (Huang JH et al., 2022). The upper mantle beneath the Luxi Uplift exhibits low resistivity, with asthenospheric upwelling along the western branch of the Tanlu Fault Zone on its eastern side (Ye GF et al., 2021). The lower crust and upper mantle of the Trans-North China Orogen exhibit low-resistivity horizontal layers, providing evidence for crust-mantle decoupling and magma underplating (Yang XZ et al., 2008). In the Western Block, the modification of the lithosphere beneath the northern Ordos Block and the lithosphere thinning beneath the Hetao Graben are the consequences of mantle upwelling during the Middle to Late Mesozoic (Dong H et al., 2014). According to exploring structures using MT methods, extensive low-resistivity layers are observed globally in the crust and upper mantle (Wei WB et al., 2001; Unsworth MJ et al., 2005; Johansen SE et al., 2019; Li BC et al., 2020; Egbert GD et al., 2022). However, significant controversy exists regarding interpreting these low-resistivity anomalies within the lithosphere. Currently, the explanations for low-resistivity anomalies in the lithosphere include the structural water in nominally anhydrous minerals (NAMs) (Yoshino T et al., 2008), the pore-network model (Cai JC et al., 2017), positive hole pairs (PHPs) (Freund F, 2003), sulfur (Ducea MN and Park SK, 2000; Virtanen VJ et al., 2021; Dong H et al., 2014), and graphite film (Duba AG and Shankland TJ, 1982; Yoshino T and Noritake F, 2011; Guo YX et al., 2021), among other models. However, the current research lacks a quantitative explanation for the low-resistivity anomalies in the lithosphere.

The water content of the lithospheric mantle is closely related to the stability of the NCC, and high water content can induce cratonic destruction (Xia QK et al., 2013). Therefore, the results of rock physics experiments have provided a quantitative conductivity-temperature relationship between the highly interconnected grain boundary melt and the NAMs. This relationship enables us to infer the thermal state and distribution of fluids (melt and volatiles) at the lithosphere. Based on this method, scholars have utilized NAMs to explain the low-resistivity anomalies observed in different regions of the upper mantle. These include asthenospheric upwelling material (Ledo J and Jones AG, 2005), magma beneath volcanoes (Hill GJ et al., 2015; Hata M et al., 2016; Gao J et al., 2020), partial melting caused by volatile water and carbon dioxide in subduction zones (Peacock SA, 1990), and saline fluids (Glover PWJ and Vine FJ, 1994). This paper

investigates the process and state of lithospheric destruction in the NCC by comparing the calculated resistivity of the cratonic lithosphere by the rock physics experiments with the resistivity model obtained from the three-dimensional (3-D) inversion of MT data. The study utilizes the mineral composition of mantle xenoliths from the NCC and the lithospheric temperature. The Nernst-Einstein and Arrhenius equations for the conductivity-temperature relationship are computational principles. Calculation parameters include volatile water and carbon dioxide. Then, the authors discuss the difference between the theoretical calculation of the cratonic lithospheric resistivity and the resistivity model from MT methods.

2. Method

2.1. Conductivity-temperature relationship of monophase minerals

The low resistivity of the crust and mantle is attributed to fluids such as water, carbon dioxide, and molten materials. Structural water can exist in minerals, while pore water can be found in rocks. They are defined as the water-bearing mineral and pore-network models.

Structural water exists in NAMs as OH^- and H_2O in the water-bearing mineral model. NAMs include olivine (Ol), orthopyroxene (Opx), clinopyroxene (Cpx), garnet (Grt), and plagioclase (Pl). The rock physics experiment measured the resistivity of these silicate minerals and studied the role of charged particles as carrier charges. The experiments revealed that proton conduction is the dominant mechanism under hydrated conditions. In contrast, ionic conduction and small polaron conduction are the primary mechanisms under anhydrous conditions (Figs. 2a, b).

In the pore-network model, water and carbon dioxide in rock pores also contribute to low resistivity due to ionic conduction (Sifré D et al., 2014). However, there is a debate about whether pore fluids can persist over the long term under solid-phase conditions. As the temperature increases, minerals melt and become fluids. The melt can accelerate the sliding of grain boundaries. Simultaneously, structural water in minerals enters the melt after dissolving. When the melt fraction reaches a threshold, the grain boundary becomes highly interconnected, forming a grain boundary melt model (Shankland TJ, 1977; Gaillard F et al., 2008; Yoshino T et al., 2010), which significantly reduces the bulk resistivity of rocks (Fig. 2c).

When the bulk rock remains unmelted, the conductive model is based on a water-bearing mineral model (NAMs). When solid minerals reach a threshold temperature, their insulating properties transform into semiconducting properties. Considering the pore-network model and performing calculations for the solid-melt systems is necessary. First, the calculation of conductivity and temperature is considered for monophase minerals, where the concentration, valence, and migration of charge carriers determine the conductivity mechanism of solid minerals and melts. The conductivity of charge carriers is calculated using the Nernst-Einstein equation (Kubo R, 1966):

$$\sigma_i = \frac{D_i z_i^2 N_i}{kTH_R} \tag{1}$$

where σ_i, D_i, z_i and N_i are the conductivity (S/m), diffusion coefficient (m^2/s), valence (C), and concentration (m^{-3}) of the ith charge carrier, respectively. k is the Boltzmann constant (k=1.38 × 10^{-23} J/K), T is the absolute temperature (K), and H_R (Haven ratio) is determined by the conduction mechanism (Haven Y and Verkerk B, 1965). Through laboratory research, the logarithm of the conductivity exhibits a linear relationship with the reciprocal of temperature within a specific temperature range, which can be described by the Arrhenius equation (Tyburczy JA and Waff HS, 1983; Roberts JJ and Tyburczy JA, 1999):

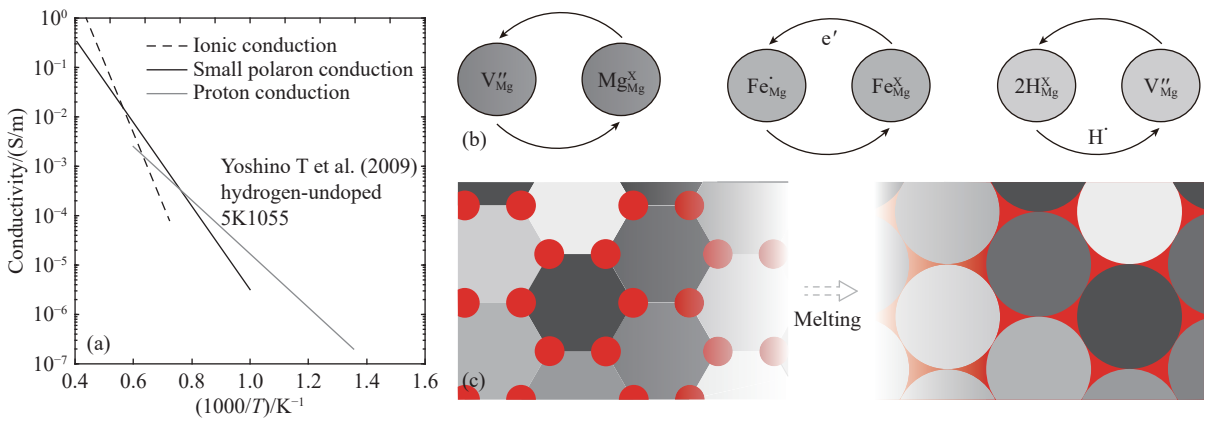

Fig. 2. a–Conductivity-temperature relationship of hydrogen-undoped olivine (after Yoshino T et al., 2009); b–schematic illustration of the conductive mechanism of minerals (after Yoshino T et al., 2008; Selway K, 2014) (V stands for electron holes. ′ stands for a negative charge. x stands for a neutral charge. And • stands for a positive charge. Ionic conduction is the conduction of iron or magnesium ions with electron holes and has a high activation enthalpy. Small polaron conduction is the conduction of electrons between Fe^{2+} and Fe^{3+}, with a medium activation enthalpy. Proton conduction is the diffusion of hydrogen ions, and the activation enthalpy is the lowest); c–schematic illustration of mineral connectivity (the red part represents the connection between the minerals).

$$\sigma = \sigma_0 \exp\left(-\frac{\Delta H}{RT}\right) = \sigma_0 \exp\left(-\frac{\Delta E + P\Delta V}{RT}\right) \quad (2)$$

where σ is the conductivity of monophase minerals (S/m), σ_0 is the pre-exponential factor of conductivity (S/m), ΔH is the activation enthalpy (kJ/mol), R is the gas constant ($R=k\cdot N_A=8.314 \times 10^{-3}$ kJ/(mol·K), N_A is the Avogadro constant), ΔE is the activation energy (kJ/mol), P is the pressure (GPa), and ΔV is an activation volume term (cm^3/mol). The remaining parameters are the same as in Eq. 1.

Under solid systems, the conduction mechanism of NAMs is associated with temperature, pressure, and volatile water. With increasing temperature, the primary conduction mechanism in olivine and orthopyroxene changes from proton conduction to small polaron conduction. Meanwhile, for anhydrous samples of clinopyroxene and garnet, the primary conduction mechanism is small polaron conduction, whereas in hydrated samples, it is proton conduction. Among the four minerals, only garnet is significantly sensitive to pressure. Due to the substantial influence of olivine on bulk conductivity, an abundance of high-temperature and high-pressure experimental data exists for olivine (Karato S, 1990; Wang DJ et al., 2006; Yoshino T et al., 2009). Analysis of the high-temperature and high-pressure experimental results for olivine, orthopyroxene, clinopyroxene, and garnet in both dry and wet conditions reveals an increase in conductivity (within the range of 10^{-6} to 10 S/m) with the rising temperature at the prescribed experimental temperature and pressure (Fig. 3).

As temperature increases, solid minerals begin to melt. The authors consider the conductivity mechanisms of silicate melts and carbonate melts. The conductivity of silicate melts primarily depends on temperature, pressure, volatiles (such as water and carbon dioxide), and the ratio of non-bridging oxygens to tetrahedral cations (NBO/T). In contrast to silicate melts, carbonate melts characterize depolymerization, resulting in a weaker dependence of carbonate conductivity on temperature and pressure. Moreover, the conductivity of carbonate melts is at least two orders of magnitude higher than silicate melts, and both the conductivity of carbonate melts and silicate melts are higher than the NAMs (Fig. 4). Notably, volatiles serve as ion conductors in silicate and carbonate melts.

2.2. Conductivity-temperature relationship of solid-melt systems

To accurately calculate the electrical conductivity of bulk rocks, it is assumed that the solid-melt systems are homogeneous and isotropic, and the proportions of minerals and water distribution control the conductivity. The Hashin-Shtrikman (*HS*) bounds provide a constraint on those parameters. The conductivity of the solid-melt systems determined by *HS* bounds is as follows (Hashin Z and Shtrikman S, 1962):

$$\sigma_{HS_\pm} \equiv \left[\sum_{i=1}^{N} \frac{v_i}{\sigma_i + 2\sigma_{max,min}}\right]^{-1} - 2\sigma_{max,min} \quad (3)$$

where $\sigma_{HS_\pm}$ is the maximum and minimum conductivity values of the upper mantle rocks (HS_+ depends on the maximum conductivity of the minerals, and HS_- depends on the minimum conductivity of minerals). N is the number of minerals in the upper mantle. v_i is the volume percentage of each mineral. $\sigma_{max,min}$ are the maximum and minimum conductivity among the minerals, and σ_i is the conductivity of each mineral. Due to the high resistivity of solid minerals, which is disconnected, the conductivity of solid minerals

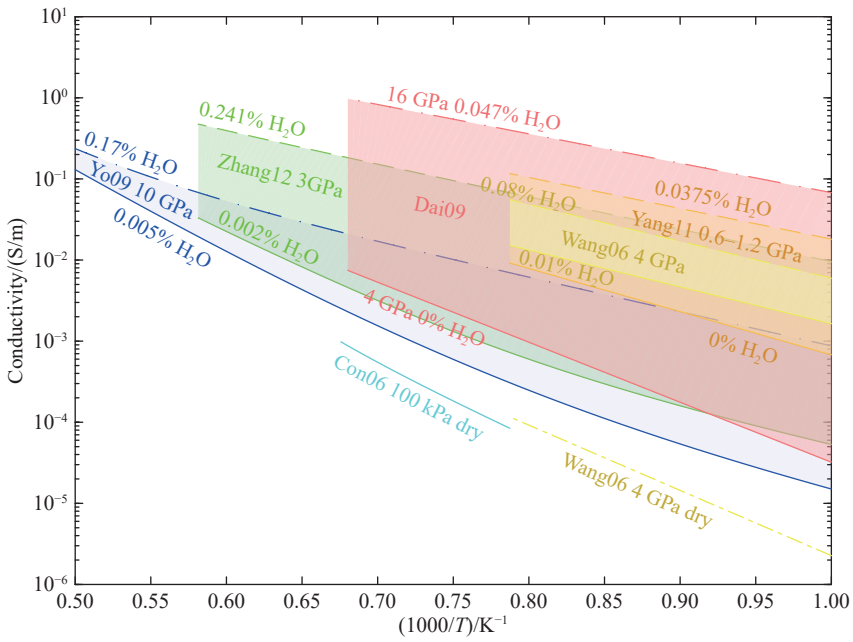

Fig. 3. Relationship between conductivity and temperature of NAMs. Data source of olivine: Yo09 (after Yoshino T et al., 2009), Wang06 (after Wang DJ et al., 2006), Con06 (after Constable S, 2006); orthopyroxene: Zhang12 (after Zhang BH et al., 2012); clinopyroxene: Yang11 (after Yang XZ et al., 2011); garnet: Dai09 (after Dai LD and Shun-ichiro K, 2009).

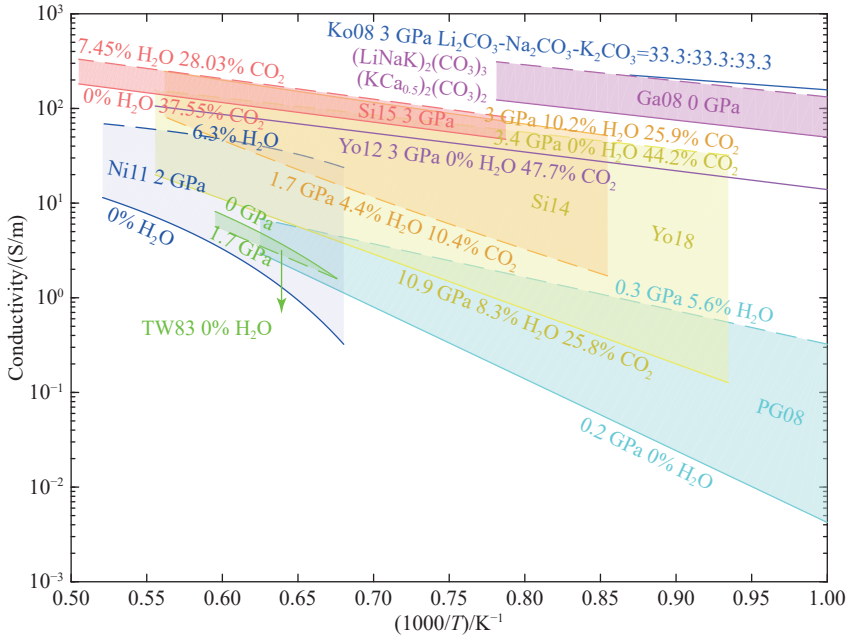

Fig. 4. Relationship between conductivity and temperature of silicate and carbonate melts. Data source of silicate melts: Ni11 (after Ni HW et al., 2011), TW83 (after Tyburczy JA and Waff HS, 1983), PG08 (after Pommier A et al., 2008); carbonate melts: Yo18 (after Yoshino T et al., 2018), Si14 (after Sifré D et al., 2014), Yo12 (after Yoshino T et al., 2012), Si15 (after Sifré D et al., 2015), Ga08 (after Gaillard F et al., 2008), Ko08 (after Kojima T et al., 2008).

takes the lower limit of the *HS* bounds (HS_-). When the temperature exceeds the solidus line, the solid minerals and melt are coexistence. Under solid-melt systems, the *HS* bounds can calculate the bulk conductivity of two-phase systems. In this case, the conductivity of the upper mantle is determined by the upper limit of the *HS* bounds (HS_+), which represents a connected liquid phase.

The conductivity mechanisms of fluids (water, carbon dioxide, and melt) exhibit disparities between solid and solid-melt systems. Structural hydroxyl (OH) and molecular water in NAMs provide conditions for proton conduction. However, the distribution of carbon dioxide in melts is considered since volatile carbon dioxide is exclusively present in melts (Keppler H et al., 2003; Stagno V et al., 2013). After the temperature rises above the threshold at which minerals become interconnected, volatile water and carbon dioxide act as carriers in the melt, providing conditions for ionic conduction.

Besides constraining the conductivity range of solid-melt systems, it is necessary to consider the distribution of volatile. When the water of the bulk rock is given, the fraction of water in NAMs and melt is different. Notably, the water distribution ratios in NAMs are as follows: Ol∶Opx∶Cpx∶Grt=1∶16∶30∶1 (Peslier AH, 2010). When the melt contains water, the distribution ratios of water in solid-melt systems are as follows: melt∶Ol∶Opx∶Cpx∶Grt=1000∶2∶3∶20∶1 (Kohn SC and Grant KJ, 2006). Quantitative relationships based on the partial melting process in lherzolite include (Katz RF et al., 2003): (1) The relationship between melt fraction, temperature, and water in the solid-melt systems; (2) calculation of the threshold temperature; (3) distribution coefficients of water between garnet lherzolite and melt.

When calculating the conductivity of solid-melt systems, the conductivity-temperature relationships of Ol (Yoshino T et al., 2009), Opx (Zhang BH et al., 2012), Cpx (Yang XZ et al., 2011), Grt (Dai LD and Shun-ichiro K, 2009), and melt (Sifré D et al., 2015) are applied. Mineral compositions in the upper mantle and the bulk water are described in Section 3.2 and Table S1. Based on the bulk conductivity-temperature relationship depicted in Fig. 5, it can be inferred that with increasing depth, the initial melting temperature increases (indicating a more challenging partial melting process). When minerals are not melting, depth (pressure) has minimal impact on the conductivity-temperature relationship. In the process of melting in the upper mantle, NAMs and hydrous minerals both contribute to the bulk conductivity. However, the structural water in NAMs significantly enhances proton conduction (Yoshino T et al., 2009). Additionally, as the temperature rises, the release of structural water from NAMs into the melt, along with carbon dioxide, facilitates ionic conduction (Sifré D et al., 2015) (Fig. 6).

3. Discussion

3.1. The 3-D resistivity model characteristics of the NCC

The "SinoProbe" project deployed an MT array in the NCC (Dong SW and Li TD, 2009). It consisted of 775 broadband MT stations and 95 broadband and long-period MT stations. The inversion for the 3-D resistivity model used a 111 (x)×181 (y)×69 (z) grid. The inversion parameters were set with an error of $|Zxy*Zyx|^{1/2}$*10% for the diagonal elements (Zxx and Zyy) and $|Zxy*Zyx|^{1/2}$*5% for the off-diagonal elements (Zxy and Zyx). The initial model used was a

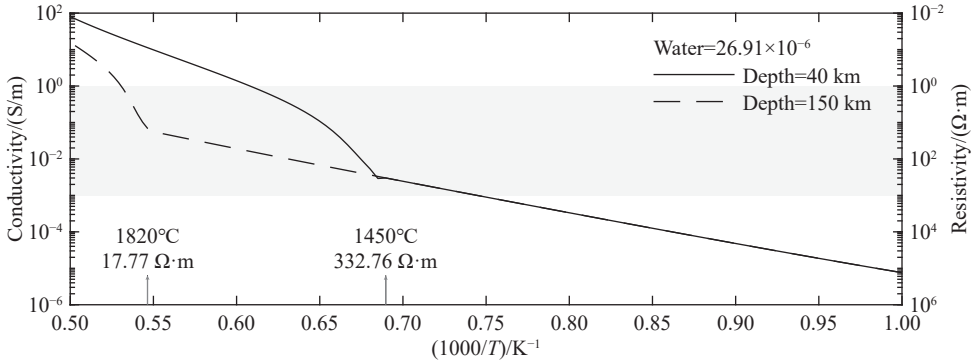

Fig. 5. Conductivity-temperature relationship of solid-melt systems. The grey regions represent the conductivity between 10^{-3} and 1 S/m. The gray arrows indicate the partial melting initiation of bulk minerals, while the numerical values within the gray box represent the temperature and resistivity during the melting of bulk minerals.

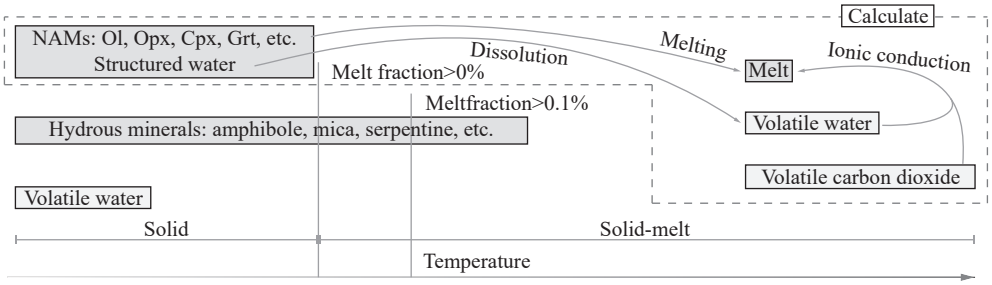

Fig. 6. Schematic diagram of dynamic changes of water and carbon dioxide during melting of upper mantle minerals. NAMs means nominally anhydrous minerals; the "Calculate" in the dashed box is the calculation category of this study; the criterion for determining mineral interconnection proposed by Hirschmann MM (2010) was applied when the melt fraction exceeded 0.1%. Ol–olivine; Opx–orthopyroxene; Cpx–clinopyroxene; Grt–garnet.

homogeneous half-space of 100 Ω·m. After 400 iterations, the RMS misfit was 2.07.

The 3-D resistivity model reveals the presence of large-scale low-resistivity anomalies in the Bohai Bay Basin and Ordos Block, which can be attributed to sedimentary deposits (Figs. 7a, b). Furthermore, with increasing depth, low-resistivity features are also observed in the northern Ordos Block in the middle and lower crust, as well as in the Yinchuan Graben (Cw1), Shanxi Graben, Weihe Graben (Cw5), and southern Taihang Uplift (Ce4). The high-resistivity and low-resistivity anomalies in the upper mantle exhibit a distinctive pattern of concentrated segmentation (Figs. 7d–g). The high-resistivity anomaly in the Alax Block (R1) is connected to the southern Ordos Block (R2), while the high-resistivity anomalies in the Yanshan Block, northern Taihang Uplift (R4), and the Sulu Orogenic Belt (R5) are interconnected. With increasing depth, the resistivity characteristics become more simplified, and the low-resistivity regions are partitioned into eastern and western parts by the North-South Gravity Lineament. The western side primarily encompasses the northern Ordos Block and the northern Trans-North China Orogen. In contrast, the eastern side mainly includes the Bohai Bay Basin, the Luxi Uplift, and the southern Taihang Uplift (Figs. 7h–j).

The low-resistivity anomalies in the upper mantle of the NCC are separated by the Taihang Uplift and North-South Gravity Lineament, indicating different origins for the low-resistivity anomalies (Li BC et al., 2019). The Eastern Block is most affected by the subduction and retreat of the Paleo-Pacific Plate, exhibiting an activated state through mantle replacement. Large-scale fluid migration and partial melting cause the widespread low resistivity observed in the crust and upper mantle. In the West Block, the low-resistivity materials beneath the northern Ordos Block in the upper mantle exhibit an upwelling trend toward surrounding grabens and rift basins. The presence of magma is confirmed by the Datong and Wulanhada volcanoes in the northeastern direction of the Ordos Block. These observations imply that the Ordos Block has been influenced by the northeastward growth of the Qinghai-Xizang Plateau, causing deep-seated thermal materials to upwell surrounding volcanoes, grabens, and basins.

3.2. Lithological characteristics of the upper mantle in the NCC

The igneous rocks (including volcanic and intrusive rocks) in the NCC and its surrounding blocks are distributed in the Yinshan-Yanshan Block, the Qinling-Dabie Orogen, the northern Trans-North China Orogen, the Jiaolai Basin and the Sulu Orogenic Belt (Fig. 1). These igneous rocks originate from both the crust and mantle, undergoing partial melting and upwelling. Petrological analysis of Cenozoic/Mesozoic basalts within the igneous provinces of the NCC suggests that Mesozoic basalts are derived from the ancient lithospheric

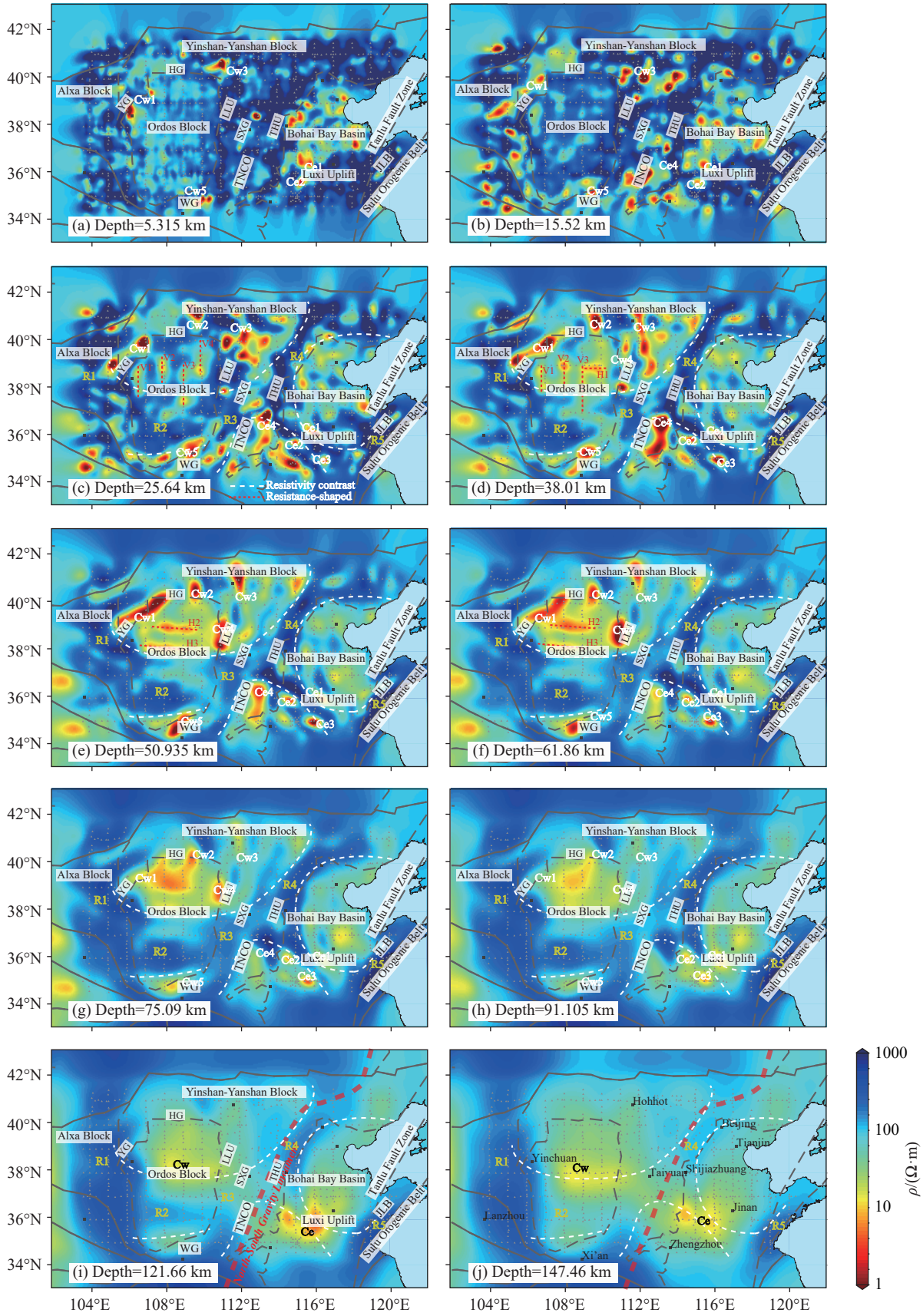

Fig. 7. 3-D resistivity model of the North China Craton shown as horizontal slices at different depths (after Li BC et al., 2019; Ye GF, 2024). The black squares represent provincial capitals, and the names of the provincial capitals are listed in (j). Ce and Cw indicate major low-resistivity anomalies (Ce consists of Ce1, Ce2, Ce3, and Ce4; Cw consists of Cw1, Cw2, Cw3, and Cw4). R1–R5 indicate major high-resistivity anomalies. YG–Yinchuan Graben; HG–Hetao Graben; WG–Weihe Graben; LLU–Lüliang Uplift; SXG–Shanxi Graben; THU–Taihang Uplift; TNCO–Trans-North China Orogen; JLB–Jiaolai Basin.

mantle. In contrast, Cenozoic basalts primarily originate from the asthenospheric mantle. This indicates that the upwelling asthenosphere replaced the ancient lithospheric mantle (Huang F et al., 2017) from the Mesozoic to Cenozoic eras. The NCC experienced subductions of the Paleo-Asian Ocean in the north, the Paleo-Tethyan Ocean in the south, and the Paleo-Pacific Plate in the east, leading to the ingress of significant amounts of hydrous and carbonate minerals into the lithospheric mantle (Wang ZX et al., 2022). During the Early Cretaceous, the westward subduction and retreat of the Paleo-Pacific Plate led to upwelling and decompression melting at the LAB (lithosphere-asthenosphere boundary) (Zhu G et al., 2012; Su XD et al., 2023). The mantle's carbon dioxide transport to the Earth's surface, facilitated by geothermal activities, magmatic events, and deep-seated faults, is observed in various carbon dioxide reservoirs, such as those in the Bohai Bay Basin (Zhao FY et al., 2017). Therefore, incorporating carbonate melts and carbon dioxide in calculations about the relationship between the resistivity structure and thermal structure of the upper mantle in the NCC is justifiable.

Analysis of mantle xenoliths in the igneous rock regions of the NCC provides insights into the state of the lithosphere. Based on the analysis of 114 spinel (Spl) lherzolite and Spl harzburgite xenoliths collected from locations, including Yangyuan, Hannuoba, Hebi, and Nvshan (Table S1), the mineral composition of the mantle consists of 66% Ol, 22% Opx, 10% Cpx, and 2% Spl and hornblende (Hbl) (Aubaud C et al., 2007; Yang XZ et al., 2008; Bonadiman C et al., 2009; Xia QK et al., 2010; Wang Q et al., 2014). Compared to other cratons, the NCC lacks garnet, which is highly pressure sensitive. In calculating the mineral composition, the authors have disregarded the minor content of Spl and Hbl, and used a proportion of 68% Ol, 22% Opx, and 10% Cpx. Moreover, the transition of mantle peridotite xenoliths from fertile lherzolite to refractory harzburgite from east to west across the NCC suggests that the eastern lithosphere is more prone to melting.

3.3. Characteristics of the fluid content of the NCC

Compared with heat flow, the 3-D thermal state at different depths reflects the current state of the lithosphere. The temperature of the NCC lithosphere was calculated using a 3-D heat conduction equation (case B) (Sun YJ et al., 2022), with parameters including heat flow, thermal conductivity, radiogenic heat production, and temperature at a depth of 100 km (An MJ and Shi YL, 2006). The average temperature was calculated for the Bohai Bay Basin (115°E–117.5°E, 37.5°N–40°N), Trans-North China Orogen (112°E–114°E, 35°N–40°N), and Ordos Block (107°E–111°E, 35°N–40°N) of the NCC (blue box in Fig. 1) (Fig. 8e). It can be seen that the temperature gradient is highest in the Bohai Bay Basin within the depth of 30–150 km, where the temperature at a depth of 150 km reaches up to 1700°C. The Trans-North China Orogen exhibits the highest temperature within a depth range of less than 80 km, followed by a rapid decrease in temperature gradient, which may be related to the dehydration and cooling of the Pacific stagnant slab (at the same depth, the higher the water, the lower the temperature required to achieve the same conductivity). The temperature in the Ordos Block is lowest at depths greater than 60 km, and its trend of temperature-depth relationship is similar to that of the Trans-North China Orogen.

Figs. 8a–c illustrate the conductivity-depth relationships for the Ordos Block, Trans-North China Orogen, and Bohai Bay Basin, respectively, using the methodology in Section 2. Although the discussion in Section 2.1 suggests that carbonate melts significantly enhance conductivity, Fig. 8c reveals a decreasing trend in conductivity at depths greater than 110 km. This can be attributed to the increasing melt content (Fig. 8f), where the carbon dioxide content within the melt reaches saturation (45%) before experiencing a substantial rise in the water/carbon dioxide ratio within the melt (Fig. 8g). The reduction in the proportion of carbon dioxide in the melt, coupled with the increase in pressure, contributes negatively to conductivity, outweighing the positive contributions arising from increased melt and water, as well as temperature elevation. The two abrupt changes observed on the conductivity-depth curve represent the results when the melt fraction reaches 0% and 0.1%, respectively. The first transition is the critical temperature at which the solid mantle transforms to the molten mantle, and higher water leads to more obverse transitions and higher conductivity. With depth increases, the transformation temperature increases, indicating a higher critical temperature for the solid mantle to molten mantle transition. Under the same depth, high water content leads to low transformation temperature, indicating a greater possibility of partial melting.

3.4. Lithosphere destruction in the NCC

The water content in the lithospheric mantle of the NCC at different times indirectly reflects the degree of destruction. Compared with the oceanic lithospheric mantle ($>50\times10^{-6}$), cratonic lithospheric mantle ($119\times10^{-6}\pm54\times10^{-6}$), and non-cratonic lithospheric mantle ($78\times10^{-6}\pm45\times10^{-6}$) (Xia QK et al., 2010), the NCC experienced stages of enhanced hydration during the Early Cretaceous (about 120 Ma) (Xia QK et al., 2013), significantly reduced hydration during the Late Cretaceous (approximately 40×10^{-6}–200×10^{-6}), and markedly dehydrated lithospheric mantle during the Cenozoic (<40 Ma) ($25\times10^{-6}\pm18\times10^{-6}$) (Yang XZ et al., 2008; Xia QK et al., 2010; Hao YT et al., 2016). Therefore, water enrichment (hydration) induces lower viscosity in the lithospheric mantle, making it more susceptible to destruction (Fig. 9a). As the destruction process concludes, the combination of lower water content and higher viscosity enhances the stability of the cratonic lithospheric mantle. In the study, the water content of 200×10^{-6} in the lithospheric mantle exceeds that of the Cenozoic lithospheric mantle in the NCC. However, only when the depth exceeds 90 km does the calculated resistivity

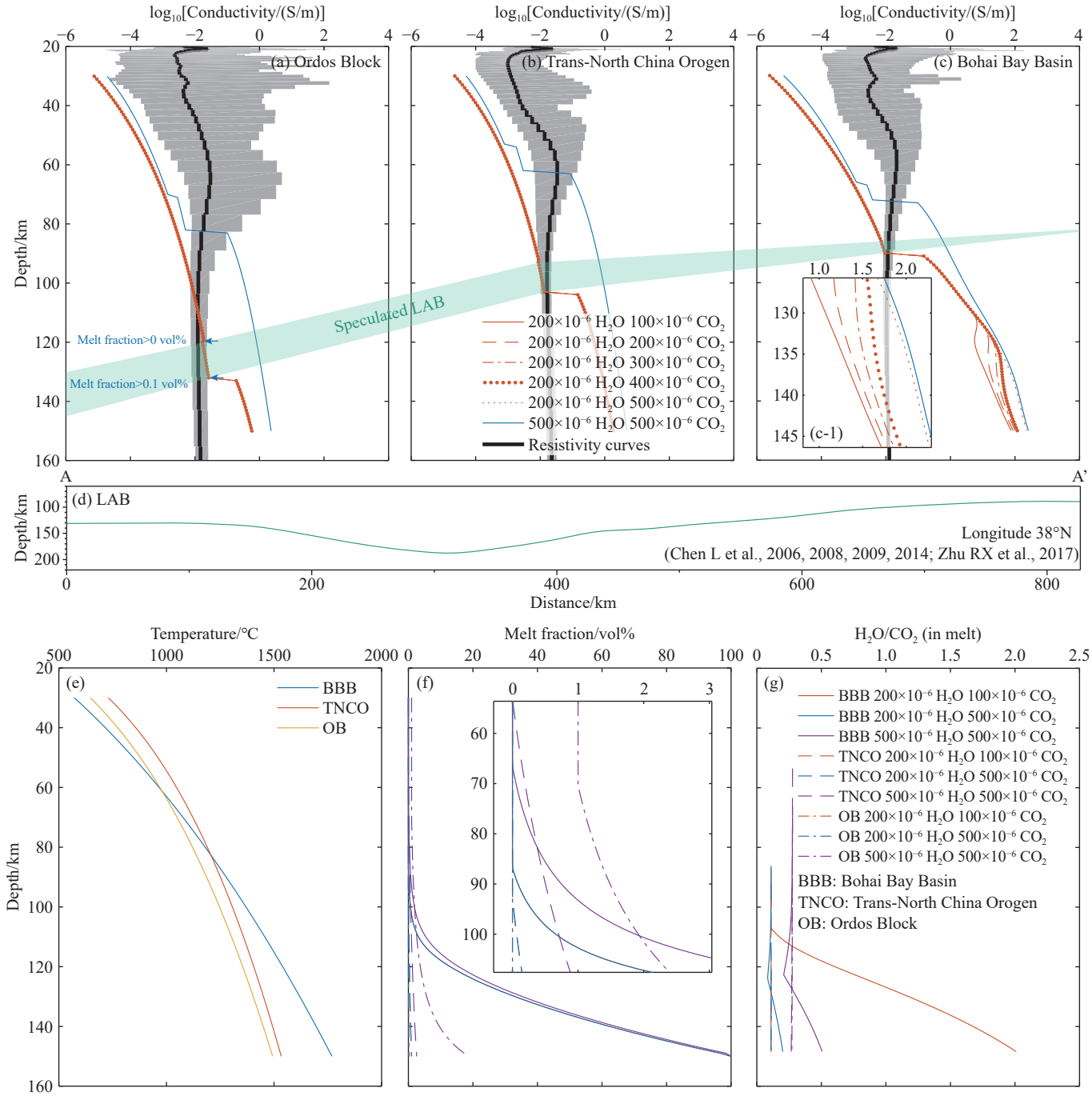

Fig. 8. a, b, c–Conductivity-temperature relationships of the Ordos Block, the Trans-North China Orogen, and the Bohai Bay Basin, respectively (Black lines and gray polygons are the average and the ranges of resistivity value of MT; the light green area is the LAB determined by the 0–0.1% melt fraction); d–depth of the LAB of the 38°N was obtained by combining seismic images with geological and geochemical constraints (after Chen L et al., 2006, 2008, 2009, 2014); e–temperature-depth relationship calculated by the steady-state heat conduction; f–melt fraction-depth relationship; g–H_2O/CO_2-depth relationship with different volatiles.

of the Bohai Bay Basin align closely with that obtained from the MT method (Fig. 8c). This implies a greater involvement of carbon dioxide in the melt's conductivity, providing a more suitable explanation for the high conductivity. The source of carbon dioxide is associated with the volatile release of carbon dioxide during the subduction of Paleo-Pacific plate sediments into the lithospheric mantle (Plank T and Manning CE, 2019).

The comparative analysis of the lithospheric mantle conductivity among three tectonic blocks shows that the gradient change of the conductivity-depth curve derived from the MT method in the Bohai Bay Basin is relatively smaller than that of the temperature curve. It indicates the complex origin of high conductivity in the Bohai Bay Basin, which has experienced significant destruction. Moreover, it highlights the considerable variations in the distribution of water, carbon dioxide, and melts with increasing depth. The difference in water content between the crust and lithospheric mantle in the

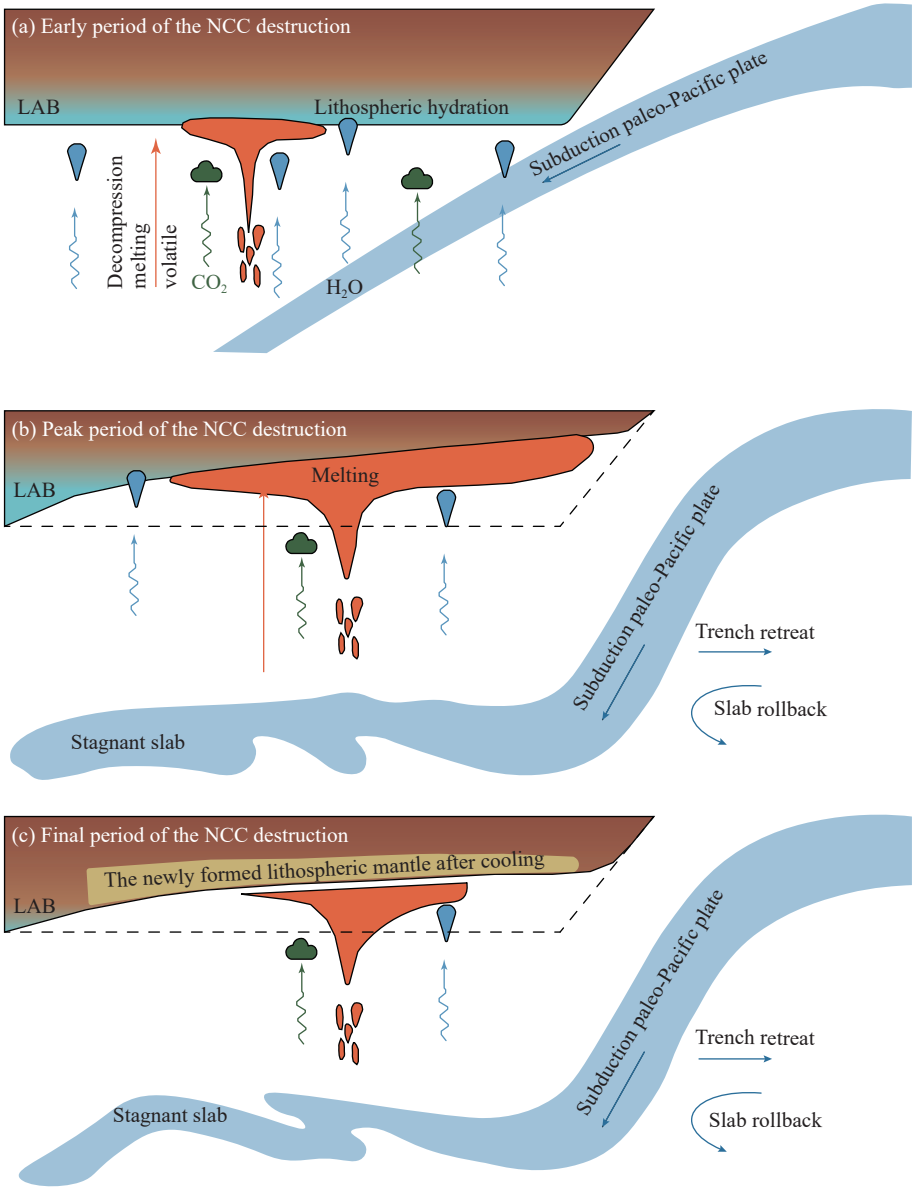

Fig. 9. A schematic illustration of hydration and thermal erosion in the North China Craton lithosphere.

Bohai Bay Basin and the Trans-North China Orogen suggests decoupling at the crust-mantle interface (Yang XZ et al., 2008), which excludes the delamination for explaining lithospheric thinning. Furthermore, when the water content reaches 200×10^{-6}, partial melting initiates at approximately 130 km depth in the Ordos Block, around 100 km depth in the Trans-North China Orogen, and nearly 90 km depth in the Bohai Bay Basin. This reflects the depth of the LAB (shallow green area in Fig. 8) and the gradual thinning of the North China Craton lithosphere from west to east.

Based on the 3-D resistivity model from the MT method and the calculated conductivity from rock physics experiments, the authors analyze the destruction process of the NCC. During the Late Mesozoic, the Paleo-Pacific plate beneath the NCC subducted and retreated, and the stagnant slab in the mantle transition zone was dehydrated (Niu YL, 2005). Subsequently, the hydrous asthenosphere upwelled and eroded the lithospheric mantle and induced partial melting under hydrous and depressurized conditions (Li P et al., 2015). Furthermore, the hydrous lithospheric mantle provided a low-viscosity state contributing to the destruction (Xia QK et al., 2013). The combined hydration and thermal erosion processes in the lithospheric mantle destructed the eastern NCC (Fig. 9b). As the destruction process persisted, the overlying lithospheric mantle underwent continuous heating. Eventually, the lithospheric mantle was destructed entirely during the Late Mesozoic, leading to thinning and dehydration. The upwelling asthenosphere subsequently cooled and accreted, forming a new lithospheric mantle (Xia QK et al., 2019) (Fig. 9c). Consequently, the water content within this newly formed lithospheric mantle might be higher than that of the dehydrated remnants of the old cratonic lithospheric mantle. This rheological contrast may have influenced the thermal evolution, resulting in the present-day low geothermal gradient observed at shallow depths in the Bohai Bay Basin.

Analyzing the current state of the NCC lithospheric mantle, it is suggested that the low-resistivity anomalies in the eastern NCC by the MT method are attributed to partial melting, as well as higher water and carbon dioxide content than those indicated in Fig. 8. The Paleo-Asian oceanic subduction has affected the northern Trans-North China Orogen, with the remaining oceanic crust providing carbon dioxide into the lithosphere (Zheng TY et al., 2009; Chen CF et al., 2016). However, using carbon dioxide to explain the large-scale low-resistivity anomalies of the lithosphere is not reasonable. Although the resistivity of the middle and lower crust of the Ordos Block based on the MT method is high, the resistivity of the lithospheric mantle is similar to that of the Bohai Bay Basin and the Trans-North China Orogen. Notably, extensive low-resistivity anomalies are distributed in the northern Ordos Block (north of 37.5°N). The Ordos Block may have been activated by the far-field effects of the collision between the Indian and Eurasian plates, resulting in a high melt fraction. The flat surface features in the northern Ordos Block suggest the presence of extensive fluids underground, which have balanced the surface relief (Fu RS et al., 1994). Simultaneously, the retreat of the Paleo-Pacific Plate has reactivated the old structures within the NCC, providing favorable conditions for the upwelling of deep-seated materials. Furthermore, from the slices of the 3-D resistivity model in Fig. 7, the low-resistivity anomalies in the deep northern Ordos Block tend to upwell towards the surrounding grabens and basins. It explains the source of the magma for the Hohhot-Jining-Datong volcanic magma. Additionally, the shallow region (<60 km) is not characterized by low temperature; in fact, it is even higher than that of the Bohai Bay Basin (Fig. 8e), thus challenging the previous understanding of the Ordos Block of low temperature, stability, and rigid lithospheric block (Ren ZL et al., 2007).

4. Conclusions

The lithospheric destruction of the NCC was studied through integrated analysis of MT data, mineral physics calculations, and mantle xenolith constraints. The main findings are as follows.

(i) The NCC exhibits significant east–west heterogeneity in lithospheric state, delineated by the North–South Gravity Lineament. The eastern domain (Bohai Bay Basin and Luxi Uplift) is characterized by widespread low-resistivity anomalies in the upper mantle, indicating intensive destruction, whereas the western domain (Ordos Block) retains features of a more stable craton.

(ii) Low-resistivity anomalies (<10 Ω·m) are extensively distributed in the lithosphere across multiple tectonic units, including the northern Ordos Block, the Yinchuan–Shanxi–Weihe Graben systems, the southern Taihang Uplift, and the Bohai Bay Basin, suggesting that the destruction process has left a pervasive electrical signature throughout the lithosphere.

(iii) Quantitative modeling based on the Arrhenius equation and *HS* bounds reveals that elevated volatile contents (H_2O and CO_2) in mantle fluids significantly lower the solidus temperature of the lithospheric mantle. The resulting hydration and partial melting reduce lithospheric strength, making it more susceptible to destruction. Therefore, high volatile content in mantle fluids is identified as a direct cause of lithospheric destruction in the NCC.

CRediT authorship contribution statement

Bao-chun Li, Gao-feng Ye and Le-tian Zhang conceived of the presented idea. Bao-chun Li and Gao-feng Ye inverted the MT data. Bao-chun Li and Le-tian Zhang calculated the conductivity-temperature relationship. All authors discussed the results and contributed to the final manuscript.

Declaration of competing interest

The authors declare no conflicts of interest.

Acknowledgment

This research was supported by the National Key R&D Plan (2022YFF0800702), project SINOPROBE on sub-project SINOPROBE-01, the Science and Technology Project of Inner Mongolia (2023QN04007).

Supplementary dataset

Supplementary data (Table S1) to this article can be found online at doi: 10.31035/cg2024038.

References

An MJ, Shi YL. 2006. Lithospheric thickness of the Chinese Continent. Physics of the Earth and Planetary Interiors, 159(3–4), 257–266. doi: 10.1016/j.pepi.2006.08.002.

Aubaud C, Withers AC, Hirschmann MM, Guan Y, Leshin LA, Mackwell SJ, Bell DR. 2007. Intercalibration of FTIR and SIMS for hydrogen measurements in glasses and nominally anhydrous minerals. American Mineralogist, 92(5–6), 811–828. doi: 10.2138/am.2007.2248.

Bonadiman C, Hao YT, Coltorti M, Dallai L, Faccini B, Huang YX. 2009. Water contents of pyroxenes in intraplate lithospheric mantle. European Journal of Mineralogy, 21(3), 637–647. doi: 10.1127/0935-1221/2009/0021-1935.

Cai JC, Wei W, Hu XY, Wood DA. 2017. Electrical conductivity models in saturated porous media: A review. Earth-Science Reviews, 171, 419–433. doi: 10.1016/j.earscirev.2017.06.013.

Chen CF, Liu YS, Foley SF, Ducea MN, He DT, Hu ZC, Chen W, Zong KQ. 2016. Paleo-Asian oceanic slab under the North China Craton revealed by carbonatites derived from subducted limestones. Geology, 44(12), 1039–1042. doi: 10.1130/g38365.1.

Chen L, Cheng C, Wei ZG. 2009. Seismic evidence for significant lateral variations in lithospheric thickness beneath the central and western North China Craton. Earth and Planetary Science Letters, 286(1–2), 171–183. doi: 10.1016/j.epsl.2009.06.022.

Chen L, Jiang M, Yang J, Wei Z, Liu C, Ling Y. 2014. Presence of an intralithospheric discontinuity in the central and western North China Craton: Implications for destruction of the craton. Geology, 42(3), 223–226. doi: 10.1130/G35010.1.

Chen L, Tao W, Zhao L, Zheng TY. 2008. Distinct lateral variation of

lithospheric thickness in the northeastern North China Craton. Earth and Planetary Science Letters, 267(1–2), 56–68. doi: 10.1016/j.epsl.2007.11.024.

Chen L, Zheng TY, Xu WW. 2006. A thinned lithospheric image of the Tanlu Fault Zone, Eastern China: Constructed from wave equation based receiver function migration. Journal of Geophysical Research (Solid Earth), 111(B9), B09312. doi: 10.1029/2005JB003974.

Chen XB, Zang SX, Wei RQ. 2011. Is the stable Ordos block migrating as an entire block? Chinese Journal of Geophysics, 54(7), 1750–1757 (in Chinese with English abstract). doi: 10.3969/j.issn.0001-5733.2011.07.008.

Constable S. 2006. SEO3: A new model of olivine electrical conductivity. Geophysical Journal International, 166(1), 435–437. doi: 10.1111/j.1365-246x.2006.03041.x.

Dai LD, Karato SI. 2009. Electrical conductivity of pyrope-rich garnet at high temperature and high pressure. Physics of the Earth and Planetary Interiors, 176(1–2), 83–88. doi: 10.1016/j.pepi.2009.04.002.

Deng JF, Mo XX, Zhao HL, Luo ZH, Du YS. 1994. Lithosphere root/de-rooting and activation of the East China continent. Geoscience, (3), 349–356.

Dong H, Wei WB, Ye GF, Jin S, Jones AG, Jing JN, Zhang LT, Xie CL, Zhang F, Wang H. 2014. Three-dimensional electrical structure of the crust and upper mantle in Ordos Block and adjacent area: Evidence of regional lithospheric modification. Geochemistry, Geophysics, Geosystems, 15(6), 2414–2425. doi: 10.1002/2014gc005270.

Dong SW, Li TD. 2009. SinoProbe: The exploration of the deep interior beneath the Chinese continent. Acta Geologica Sinica, 83(7), 895–909 (in Chinese with English abstract). doi: 10.3321/j.issn:0001-5717.2009.07.001.

Duba AG, Shankland TJ. 1982. Free carbon & electrical conductivity in the Earth's mantle. Geophysical Research Letters, 9(11), 1271–1274. doi: 10.1029/gl009i011p01271.

Ducea MN, Park SK. 2000. Enhanced mantle conductivity from sulfide minerals, southern sierra Nevada, California. Geophysical Research Letters, 27(16), 2405–2408. doi: 10.1029/2000gl011565.

Egbert GD, Yang B, Bedrosian PA, Key K, Livelybrooks DW, Schultz A, Kelbert A, Parris B. 2022. Fluid transport and storage in the Cascadia forearc influenced by overriding plate lithology. Nature Geoscience, 15, 677–682. doi: 10.1038/s41561-022-00981-8.

Freund F. 2003. On the electrical conductivity structure of the stable continental crust. Journal of Geodynamics, 35(3), 353–388. doi: 10.1016/S0264-3707(02)00154-0.

Fu RS, Chang XH, Huang JH, Liu WZ. 1994. Regional gravity isostatic anomaly and small scale convection model in upper mantle. Chinese Journal of Geophysics (Acta Geophysica Sinica), 37(S2), 249–258.

Gaillard F, Malki M, Iacono-Marziano G, Pichavant M, Scaillet B. 2008. Carbonatite melts and electrical conductivity in the asthenosphere. Science, 322(5906), 1363–1365. doi: 10.1126/science.1164446.

Gao J, Zhang HJ, Zhang SQ, Xin HL, Li ZW, Tian W, Bao F, Cheng ZP, Jia XF, Fu L. 2020. Magma recharging beneath the Weishan volcano of the intraplate Wudalianchi volcanic field, Northeast China, implied from 3-D magnetotelluric imaging. Geology, 48(9), 913–918. doi: 10.1130/G47531.1.

Gao S, Zhang JF, Xu WL, Liu YS. 2009. Delamination and destruction of the North China Craton. Chinese Science Bulletin, 54(19), 3367–3378. doi: 10.1007/s11434-009-0395-9.

Glover PWJ, Vine FJ. 1994. Electrical conductivity of the continental crust. Geophysical Research Letters, 21(22), 2357–2360. doi: 10.1029/94gl01015.

Guo YX, Zhu T, Zheng J. 2021. Numerical simulation of electrical conductivity on the graphite-quartz model and its geophysical application. Chinese Journal of Geophysics, 64(11), 4031–4042 (in Chinese with English abstract). doi: 10.6038/cjg2021O0487.

Hao YT, Xia QK, Jia ZB, Zhao QC, Li P, Feng M, Liu SC. 2016. Regional heterogeneity in the water content of the Cenozoic lithospheric mantle of Eastern China. Journal of Geophysical Research: Solid Earth, 121(2), 517–537. doi: 10.1002/2015jb012105.

Hashin Z, Shtrikman S. 1962. A variational approach to the theory of the elastic behaviour of polycrystals. Journal of Mechanics Physics of Solids, 10(4), 343–352. doi: 10.1016/0022-5096(62)90005-4.

Hata M, Takakura S, Matsushima N, Hashimoto T, Utsugi M. 2016. Crustal magma pathway beneath Aso caldera inferred from three-dimensional electrical resistivity structure. Geophysical Research Letters, 43(20), 10720–10727. doi: 10.1002/2016gl070315.

Haven, Y, Verkerk, B. 1965. Diffusion and electrical conductivity of sodium ions in sodium silicate glasses. Phys. Chem. Glasses, 6(2), 38–45.

Hill GJ, Bibby HM, Ogawa Y, Wallin EL, Bennie SL, Caldwell TG, Keys H, Bertrand EA, Heise W. 2015. Structure of the Tongariro volcanic system: Insights from magnetotelluric imaging. Earth and Planetary Science Letters, 432, 115–125. doi: 10.1016/j.epsl.2015.10.003.

Hirschmann MM. 2010. Partial melt in the oceanic low velocity zone. Physics of the Earth and Planetary Interiors, 179(1–2), 60–71. doi: 10.1016/j.pepi.2009.12.003.

Huang F, Xu JF, Liu YS, Li J, Chen JL, Li XY. 2017. Re–Os isotope evidence from Mesozoic and Cenozoic basalts for secular evolution of the mantle beneath the North China Craton. Contributions to Mineralogy and Petrology, 172(5), 28. doi: 10.1007/s00410-017-1342-4.

Huang JH, Yin YT, Jin S, Wei WB, Ye GF, Jing JE, Dong H, Zhang LT, Xie CL, Xu LY. 2022. 3-D electrical structure of the lithosphere beneath the Yanshan Belt and its adjacent areas, North China. Tectonophysics, 832, 229333. doi: 10.1016/j.tecto.2022.229333.

Johansen SE, Panzner M, Mittet R, Amundsen HEF, Lim A, Vik E, Landrø M, Arntsen B. 2019. Deep electrical imaging of the ultraslow-spreading mohns ridge. Nature, 567(7748), 379–383. doi: 10.1038/s41586-019-1010-0.

Karato S. 1990. The role of hydrogen in the electrical conductivity of the upper mantle. Nature, 347(6290), 272–273. doi: 10.1038/347272a0.

Katz RF, Spiegelman M, Langmuir CH. 2003. A new parameterization of hydrous mantle melting. Geochemistry, Geophysics, Geosystems, 4(9), 2002GC000433. doi: 10.1029/2002gc000433.

Keppler H, Wiedenbeck M, Shcheka SS. 2003. Carbon solubility in olivine and the mode of carbon storage in the Earth's mantle. Nature, 424(6947), 414–416. doi: 10.1038/nature01828.

Kohn SC. 2006. The partitioning of water between nominally anhydrous minerals and silicate melts. Reviews in Mineralogy and Geochemistry, 62(1), 231–241. doi: 10.2138/rmg.2006.62.10.

Kojima T, Miyazaki Y, Nomura K, Tanimoto K. 2008. Density, surface tension, and electrical conductivity of ternary molten carbonate system Li_2CO_3–Na_2CO_3–K_2CO_3 and methods for their estimation. Journal of the Electrochemical Society, 155(7), F150. doi: 10.1149/1.2917212.

Kubo R. 1966. The fluctuation-dissipation theorem. Reports on Progress in Physics, 29(1), 255–284. doi: 10.1088/0034-4885/29/1/306.

Ledo J, Jones AG. 2005. Upper mantle temperature determined from combining mineral composition, electrical conductivity laboratory studies and magnetotelluric field observations: Application to the intermontane belt, Northern Canadian Cordillera. Earth and Planetary Science Letters, 236(1–2), 258–268. doi: 10.1016/j.epsl.2005.01.044.

Li BC, Ye GF, Zhang LT, Wei WB, Jin S. 2019. Temperature analysis of the upper mantle in the North China Craton based on a three-dimensional magnetotelluric conductivity model international Workshop on Gravity, Electrical & Magnetic Methods and Their Applications, Xi'an, China, May 2019. Society of Exploration

Geophysicists and Chinese Geophysical Society, 19–22. doi: 10.1190/gem2019-008.1.

Li BC, Zhang LT, Ye GF, Jin S, Wei WB, Xie CL, Chen XR. 2020. Upper mantle thermal structure beneath the eastern margin of the Tibetan Plateau inferred from electrical structure model. Chinese Journal of Geophysics, 63(3), 1043–1055 (in Chinese with English abstract).

Li P, Xia QK, Deloule E, Chen H, Gu XY, Feng M. 2015. Temporal variation of H_2O content in the lithospheric mantle beneath the eastern North China Craton: Implications for the destruction of cratons. Gondwana Research, 28(1), 276–287. doi: 10.1016/j.gr.2014.03.012.

Menzies MA, Fan WM, Zhang M. 1993. Palaeozoic and Cenozoic lithoprobes and the loss of >120 km of Archaean lithosphere, Sino-Korean craton, China. Geological Society, London, Special Publications, 76(1), 71–81. doi: 10.1144/gsl.sp.1993.076.01.04.

Ni HW, Keppler H, Behrens H. 2011. Electrical conductivity of hydrous basaltic melts: Implications for partial melting in the upper mantle. Contributions to Mineralogy and Petrology, 162(3), 637–650. doi: 10.1007/s00410-011-0617-4.

Niu YL. 2005. Generation and evolution of basaltic magmas: Some basic concepts and a new view on the origin of Mesozoic-Cenozoic basaltic volcanism in eastern China. Geological Journal of China Universities, 11(1), 9–46.

Peacock SM. 1990. Fluid processes in subduction zones. Science, 248(4953), 329–337. doi: 10.1126/science.248.4953.329.

Peslier AH. 2010. A review of water contents of nominally anhydrous natural minerals in the mantles of Earth, Mars and the Moon. Journal of Volcanology and Geothermal Research, 197(1–4), 239–258. doi: 10.1016/j.jvolgeores.2009.10.006.

Plank T, Manning CE. 2019. Subducting carbon. Nature, 574(7778), 343–352. doi: 10.1038/s41586-019-1643-z.

Pommier A, Gaillard F, Pichavant M, Scaillet B. 2008. Laboratory measurements of electrical conductivities of hydrous and dry Mount Vesuvius melts under pressure. Journal of Geophysical Research: Solid Earth, 113(B5), 2007JB005269. doi: 10.1029/2007jb005269.

Ren ZL, Zhang S, Gao SL, Cui JP, Xiao YY, Xiao H. 2007. Tectonic thermal history and its significance on the formation of oil and gas accumulation and mineral deposit in Ordos Basin. Science in China Series D: Earth Sciences, 50(2), 27–38. doi: 10.1007/s11430-007-6022-1.

Roberts JJ, Tyburczy JA. 1999. Partial-melt electrical conductivity: Influence of melt composition. Journal of Geophysical Research: Solid Earth, 104(B4), 7055–7065. doi: 10.1029/1998jb900111.

Selway K. 2014. On the causes of electrical conductivity anomalies in tectonically stable lithosphere. Surveys in Geophysics, 35(1), 219–257. doi: 10.1007/s10712-013-9235-1.

Shankland TJ, Waff HS. 1977. Partial melting and electrical conductivity anomalies in the upper mantle. Journal of Geophysical Research, 82(33), 5409–5417. doi: 10.1029/jb082i033p05409.

Sifré D, Gardés E, Massuyeau M, Hashim L, Hier-Majumder S, Gaillard F. 2014. Electrical conductivity during incipient melting in the oceanic low-velocity zone. Nature, 509(7498), 81–85. doi: 10.1038/nature13245.

Sifré D, Hashim L, Gaillard F. 2015. Effects of temperature, pressure and chemical compositions on the electrical conductivity of carbonated melts and its relationship with viscosity. Chemical Geology, 418, 189–197. doi: 10.1016/j.chemgeo.2014.09.022.

Stagno V, Ojwang DO, McCammon CA, Frost DJ. 2013. The oxidation state of the mantle and the extraction of carbon from Earth's interior. Nature, 493(7430), 84–88. doi: 10.1038/nature11679.

Su JB, Zhu WB, Chen J, Ge RF, Zheng BH, Min B. 2014. Cenozoic inversion of the East China Sea shelf basin: Implications for reconstructing Cenozoic tectonics of Eastern China. International Geology Review, 56(12), 1541–1555. doi: 10.1080/00206814.2014.951004.

Su XD, Ping JH, Leng W, Zhao JC, Tang YJ, Liu JQ. 2023. Magma system and equilibrium depth of the Cenozoic basalts in the central North China Craton. Lithos, 446, 107142. doi: 10.1016/j.lithos.2023.107142.

Sun YJ, Dong SW, Wang XQ, Liu M, Zhang H, Shi YL. 2022. Three-dimensional thermal structure of East Asian continental lithosphere. Journal of Geophysical Research: Solid Earth, 127(5), e2021JB023432. doi: 10.1029/2021jb023432.

Tyburczy JA, Waff HS. 1983. Electrical conductivity of molten basalt and andesite to 25 kilobars pressure: Geophysical significance and implications for charge transport and melt structure. Journal of Geophysical Research: Solid Earth, 88(B3), 2413–2430. doi: 10.1029/jb088ib03p02413.

Unsworth MJ, Jones AG, Wei W, Marquis G, Gokarn SG, Spratt JE, The I-MTt, Bedrosian P, Booker J, Leshou C, Clarke G, Shenghui L, Chanhong L, Ming D, Sheng J, Solon K, Handong T, Ledo J, Roberts B. 2005. Crustal rheology of the Himalaya and Southern Tibet inferred from magnetotelluric data. Nature, 438, 78. doi: 10.1038/nature04154.

Virtanen VJ, Heinonen JS, Molnár F, Schmidt MW, Marxer F, Skyttä P, Kueter N, Moslova K. 2021. Fluids as primary carriers of sulphur and copper in magmatic assimilation. Nature Communications, 12(1), 6609. doi: 10.1038/s41467-021-26969-3.

Wang DJ, Mookherjee M, Xu YS, Karato SI. 2006. The effect of water on the electrical conductivity of olivine. Nature, 443(7114), 977–980. doi: 10.1038/nature05256.

Wang Q, Bagdassarov N, Xia QK, Zhu BB. 2014. Water contents and electrical conductivity of peridotite xenoliths from the North China Craton: Implications for water distribution in the upper mantle. Lithos, 189, 105–126. doi: 10.1016/j.lithos.2013.08.005.

Wang ZX, Liu SG, Li SG, Liu D, Liu JG. 2022. Linking deep CO_2 outgassing to cratonic destruction. National Science Review, 9(6), nwac001. doi: 10.1093/nsr/nwac001.

Wei WB, Tan HD, Jin S, Deng M, Ye GF, Deng JW, Wan ZS. 2002. Conductivity structure of lithosphere in central North China: Magnetotelluric study of Yingxian-Shanghe profile. Earth Science —Journal of China University of Geosciences, 27(5), 645–660 (in Chinese with English abstract).

Wei WB, Unsworth M, Jones A, Booker J, Tan HD, Nelson D, Chen LS, Li SH, Solon K, Bedrosian P, Jin S, Deng M, Ledo J, Kay D, Roberts B. 2001. Detection of widespread fluids in the Tibetan crust by magnetotelluric studies. Science, 292(5517), 716–719. doi: 10.1126/science.1010580.

Wilde SA. 2015. Final amalgamation of the Central Asian Orogenic Belt in NE China: Paleo-Asian Ocean closure versus paleo-Pacific plate subduction —a review of the evidence. Tectonophysics, 662, 345–362. doi: 10.1016/j.tecto.2015.05.006.

Wu FY, Sun DY, Ge WC, Zhang YB, Grant ML, Wilde SA, Jahn BM. 2011. Geochronology of the Phanerozoic granitoids in northeastern China. Journal of Asian Earth Sciences, 41(1), 1–30. doi: 10.1016/j.jseaes.2010.11.014.

Wu FY, Zhao GC, Wilde SA, Sun DY. 2005. Nd isotopic constraints on crustal formation in the North China Craton. Journal of Asian Earth Sciences, 24(5), 523–545. doi: 10.1016/j.jseaes.2003.10.011.

Xia QK, Hao YT, Li P, Deloule E, Coltorti M, Dallai L, Yang XZ, Feng M. 2010. Low water content of the Cenozoic lithospheric mantle beneath the eastern part of the North China Craton. Journal of Geophysical Research: Solid Earth, 115(B7), 2009JB006694. doi: 10.1029/2009jb006694.

Xia QK, Liu J, Kovács I, Hao YT, Li P, Yang XZ, Chen H, Sheng YM. 2019. Water in the upper mantle and deep crust of Eastern China: Concentration, distribution and implications. National Science

Review, 6(1), 125–144. doi: 10.1093/nsr/nwx016.

Xia QK, Liu J, Liu SC, Kovács I, Feng M, Dang L. 2013. High water content in Mesozoic primitive basalts of the North China Craton and implications on the destruction of cratonic mantle lithosphere. Earth and Planetary Science Letters, 361, 85–97. doi: 10.1016/j.epsl.2012.11.024.

Xu YG, Huang XL, Ma JL, Wang YB, Iizuka Y, Xu JF, Wang Q, Wu XY. 2004. Crust-mantle interaction during the tectono-thermal reactivation of the North China Craton: Constraints from SHRIMP zircon U-Pb chronology and geochemistry of Mesozoic plutons from western Shandong. Contributions to Mineralogy and Petrology, 147(6), 750–767. doi: 10.1007/s00410-004-0594-y.

Yang XZ, Keppler H, McCammon C, Ni HW, Xia QK, Fan QC. 2011. Effect of water on the electrical conductivity of lower crustal clinopyroxene. Journal of Geophysical Research, 116(B4), B04208. doi: 10.1029/2010jb008010.

Yang XZ, Xia QK, Deloule E, Dallai L, Fan QC, Feng M. 2008. Water in minerals of the continental lithospheric mantle and overlying lower crust: A comparative study of peridotite and granulite xenoliths from the North China Craton. Chemical Geology, 256(1–2), 33–45. doi: 10.1016/j.chemgeo.2008.07.020.

Yang YH, Wu FY, Wilde SA, Liu XM, Zhang YB, Xie LW, Yang JH. 2009. *In situ* perovskite Sr–Nd isotopic constraints on the petrogenesis of the Ordovician Mengyin kimberlites in the North China Craton. Chemical Geology, 264(1–4), 24–42. doi: 10.1016/j.chemgeo.2009.02.011.

Ye GF. 2024. Horizontal slices and latitude sections of the 3-D lithospheric model of the North China Craton inverted with magnetotelluric array doi: 10.17632/7wx7fdzvtx.1.

Ye GF, Li BC, Jin S, Wei WB, Zhang LT, Dong H, Xie CL, Yin YT, Sun SH, Dong JE, Liu C, Yang C, Yin HX. 2024. Multistage lithospheric destruction of the North China Craton: Evidence from an MT array study. Earth and Planetary Science Letters, in preparation.

Ye GF, Liu C, Luo X, Jin S, Wei WB, Dong H, Yin YT. 2021. Dynamical significance of the Tanlu fault zone in the destruction of the North China Craton: The evidence provided by the three-dimensional magnetotelluric array study. Tectonophysics, 813, 228910. doi: 10.1016/j.tecto.2021.228910.

Yin A, Harrison TM. 2000. Geologic evolution of the Himalayan-Tibetan Orogen. Annual Review of Earth and Planetary Sciences, 28, 211–280. doi: 10.1146/annurev.earth.28.1.211.

Yoshino T, Gruber B, Reinier C. 2018. Effects of pressure and water on electrical conductivity of carbonate melt with implications for conductivity anomaly in continental mantle lithosphere. Physics of the Earth and Planetary Interiors, 281, 8–16. doi: 10.1016/j.pepi.2018.05.003.

Yoshino T, Laumonier M, McIsaac E, Katsura T. 2010. Electrical conductivity of basaltic and carbonatite melt-bearing peridotites at high pressures: Implications for melt distribution and melt fraction in the upper mantle. Earth and Planetary Science Letters, 295(3–4), 593–602. doi: 10.1016/j.epsl.2010.04.050.

Yoshino T, Manthilake G, Matsuzaki T, Katsura T. 2008. Dry mantle transition zone inferred from the conductivity of wadsleyite and ringwoodite. Nature, 451(7176), 326–329. doi: 10.1038/nature06427.

Yoshino T, Matsuzaki T, Shatskiy A, Katsura T. 2009. The effect of water on the electrical conductivity of olivine aggregates and its implications for the electrical structure of the upper mantle. Earth and Planetary Science Letters, 288(1–2), 291–300. doi: 10.1016/j.epsl.2009.09.032.

Yoshino T, McIsaac E, Laumonier M, Katsura T. 2012. Electrical conductivity of partial molten carbonate peridotite. Physics of the Earth and Planetary Interiors, 194, 1–9. doi: 10.1016/j.pepi.2012.01.005.

Yoshino T, Noritake F. 2011. Unstable graphite films on grain boundaries in crustal rocks. Earth and Planetary Science Letters, 306(3–4), 186–192. doi: 10.1016/j.epsl.2011.04.003.

Zhai MG, Santosh M. 2011. The early Precambrian odyssey of the North China Craton: A synoptic overview. Gondwana Research, 20(1), 6–25. doi: 10.1016/j.gr.2011.02.005.

Zhang BH, Yoshino T, Wu XP, Matsuzaki T, Shan SM, Katsura T. 2012. Electrical conductivity of enstatite as a function of water content: Implications for the electrical structure in the upper mantle. Earth and Planetary Science Letters, 357, 11–20. doi: 10.1016/j.epsl.2012.09.020.

Zhang HF, Ying JF, Shimoda G, Kita NT, Morishita Y, Shao J, Tang YJ. 2007. Importance of melt circulation and crust-mantle interaction in the lithospheric evolution beneath the North China Craton: Evidence from Mesozoic basalt-borne clinopyroxene xenocrysts and pyroxenite xenoliths. Lithos, 96(1–2), 67–89. doi: 10.1016/j.lithos.2006.10.002.

Zhao FY, Jiang SH, Li SZ, Cao W, Wang G, Zhang HX, Gao S. 2017. Correlation of inorganic CO_2 reservoirs in East China to subduction of (Paleo-) Pacific Plate. Earth Science Frontiers, 24(4), 370–384. doi: 10.13745/j.esf.yx.2017-3-12.

Zhao GC, Wilde SA, Cawood PA, Sun M. 2001. Archean blocks and their boundaries in the North China Craton: Lithological, geochemical, structural and P-T path constraints and tectonic evolution. Precambrian Research, 107(1–2), 45–73. doi: 10.1016/S0301-9268(00)00154-6.

Zheng TY, Zhao L, Zhu RX. 2009. New evidence from seismic imaging for subduction during assembly of the North China Craton. Geology, 37(5), 395–398. doi: 10.1130/g25600a.1.

Zhu G, Jiang DZ, Zhang BL, Chen Y. 2012. Destruction of the eastern North China Craton in a backarc setting: Evidence from crustal deformation kinematics. Gondwana Research, 22(1), 86–103. doi: 10.1016/j.gr.2011.08.005.

Zhu RX, Xu YG. 2019. The subduction of the west Pacific plate and the destruction of the North China Craton. Science China Earth Sciences, 62(9), 1340–1350. doi: 10.1007/s11430-018-9356-y.

Zhu RX, Xu YG, Zhu G, Zhang HF, Xia QK, Zheng TY. 2012. Destruction of the North China Craton. Science China Earth Sciences, 55(10), 1565–1587. doi: 10.1007/s11430-012-4516-y.

Zhu RX, Zhang HF, Zhu G, Meng QR, Fan HR, Yang JH, Wu FY, Zhang ZY, Zheng TY. 2017. Craton destruction and related resources. International Journal of Earth Sciences, 106(7), 2233–2257. doi: 10.1007/s00531-016-1441-x.